

# Rational design and synthesis of bifunctional Dibenzo[g,p]chrysene-based conjugated microporous polymers for energy storage and visible light-driven photocatalytic hydrogen evolution

Siang-Yi Chang<sup>a,1</sup>, Ahmed M. Elewa<sup>b,c,1</sup>, Mohamed Gamal Mohamed<sup>a,d,\*\*,1</sup>,  
Islam M.A. Mekhmer<sup>b,d,1</sup>, Maha Mohamed Samy<sup>a,d</sup>, Kan Zhang<sup>e</sup>, Ho-Hsiu Chou<sup>b,\*\*\*</sup>,  
Shiao-Wei Kuo<sup>a,f,\*</sup>

<sup>a</sup> Department of Materials and Optoelectronic Science, College of Semiconductor and Advanced Technology Research, Center for Functional Polymers and Supramolecular Materials, National Sun Yat-Sen University, Kaohsiung, 804, Taiwan

<sup>b</sup> Department of Chemical Engineering, National Tsing Hua University, Hsinchu, 300044, Taiwan

<sup>c</sup> Nuclear Chemistry Department, Hot Laboratories Center, Atomic Energy Authority, Cairo, 13759, Egypt

<sup>d</sup> Chemistry Department, Faculty of Science, Assiut University, Assiut, 71515, Egypt

<sup>e</sup> Research School of Polymeric Materials, School of Materials Science and Engineering, Jiangsu University, Zhenjiang, Jiangsu, 212013, PR China

<sup>f</sup> Department of Medicinal and Applied Chemistry, Kaohsiung Medical University, Kaohsiung, 807, Taiwan

## ARTICLE INFO

### Keywords:

Conjugated microporous polymers  
Dibenzo[g,p]chrysene  
Sonogashira–Hagihara coupling reaction  
Supercapacitors  
Photocatalysts  
Hydrogen evolution

## ABSTRACT

The importance of conjugated microporous polymers (CMPs) as active components in photocatalytic hydrogen evolution is growing due to its intense ultraviolet–visible (UV–vis) absorption, potent fluorescence, and high carrier transport capacity, dibenzo[g,p]chrysene shows notable photophysical and electrical features. This is because CMPs have stiff molecular structures with large  $\pi$ -conjugation. In this section, we describe our approach and syntheses of three types of polymers for the first time to determine the reactivity of dibenzo[g,p]chrysene (TBN)-based CMPs for photocatalytic H<sub>2</sub> evolution and energy storage applications. Three TBN-based CMPs, TBN-TBN (D-D), TBN-TBN-TPA (A-D), and TBN-TBN-BT (D-A), were synthesized via Sonogashira–Hagihara coupling. TBN-CMP materials were used as working electrodes for energy storage applications. The TBN-TBN-BT CMP demonstrated excellent capacity retention (98.2%) over 2000 cycles and high capacitor (130 F g<sup>-1</sup>) at 0.5 A g<sup>-1</sup>, in accordance with electrochemical performance. Furthermore, the hydrogen evolution rate (HER) results are in the following order 8452, 9800, and 3060  $\mu\text{mol g}^{-1}\text{h}^{-1}$  for TBN-TBN, TBN-TBN-TPA, and TBN-TBN-BT CMPs, respectively. These findings suggest that using TBN as an acceptor increases the number of active sites for proton reduction, thereby boosting the rate of H<sub>2</sub> evolution.

## 1. Introduction

Energy development has advanced from uncontrolled mining and demand to the current stage of utilizing renewable resources owing to growing public awareness of green technology. The importance of sustainable environmental protection is repeatedly mentioned, making energy transition and carbon reduction the targets of current research [1–10]. Therefore, developing green and sustainable energy systems

depends on hydrogen energy, which has a high combustion value, and no carbon impact is critical. Chemical energy has been used to convert solar energy to hydrogen by the photocatalytic splitting of water using semiconductor photocatalysts [11–20]. Compared with most inorganic photocatalysts, such as metal oxides, sulfides, and selenides, owing to their high activity and suitable electronic structure, organic materials such as graphitic carbon nitride (g-C<sub>3</sub>N<sub>4</sub>) [21–24], linear polymers [25, 26], metal-organic frameworks (MOFs) [27,28], and covalent organic

\* Corresponding author. Department of Materials and Optoelectronic Science, College of Semiconductor and Advanced Technology Research, Center for Functional Polymers and Supramolecular Materials, National Sun Yat-Sen University, Kaohsiung, 804, Taiwan.

\*\* Corresponding author. Chemistry Department, Faculty of Science, Assiut University, Assiut 71515, Egypt.

\*\*\* Corresponding author.

E-mail addresses: [mgamal.eldin12@yahoo.com](mailto:mgamal.eldin12@yahoo.com) (M.G. Mohamed), [hhchou@mx.nthu.edu.tw](mailto:hhchou@mx.nthu.edu.tw) (H.-H. Chou), [kuosw@faculty.nsysu.edu.tw](mailto:kuosw@faculty.nsysu.edu.tw) (S.-W. Kuo).

<sup>1</sup> These authors contributed equally.

frameworks (COFs) [29–31], and conjugated microporous polymers (CMPs) [32–35] have been extensively used reported in recent years because most inorganic photocatalysts struggle with poor visible-light activity, difficult preparation, and scarce natural resources. Recent investigations have shown that organic semiconductors represent a promising family of photocatalysts for hydrogen evolution owing to their wide range of structures, numerous synthesis methods, and modifiable electronic properties [36–38]. CMPs are amorphous organic polymeric materials that are similar, but not identical, to other common materials with crystalline covalent organic and metal-organic frameworks. Its porous structure provides abundant adsorption sites for photocatalytic reactions [39]. Furthermore, CMPs are a subclass of conjugated polymers; as the name suggests,  $\pi$ -conjugated systems exist in microporous frameworks and are built into two- or three-dimensional networks [40]. Therefore, CMPs with  $\pi$ -conjugation is endowed with a conductive function [41]. In general, CMPs can be prepared by oxidative polymerization [42,43] or coupling reactions, such as Sonogashira coupling [44,45], Suzuki coupling [46,47], Yamamoto coupling [48, 49], and other methods. Supercapacitors (SCs) are a promising type of electrochemical energy storage system that has gained popularity because of their ability to deliver high-power density and enable rapid charging and discharging. They offer exceptional stability, high power density, and environmental friendliness, making them attractive for various applications. SCs can function both as batteries and traditional capacitors by storing energy through electrostatic interactions between the electrolyte ions and the carbon electrodes [2–7]. This easily synthesized CMP materials is characterized by insolubility in most solvents, high specific surface area and porosity, high thermal stability, high carrier mobility, and strong photocatalytic activity [50–52], making it suitable for applications in gas adsorption, energy storage, luminescence, metal ion sensing, and H<sub>2</sub> production using photocatalytic water splitting [40,53]. To increase the photocatalytic effectiveness of organic semiconductors, further work is required to create new organic photocatalyst materials and improve their electrical characteristics. The use of CMPs as photocatalysts to produce hydrogen from visible light-split water was demonstrated by Cooper et al., in 2015. Since then, much attention has been paid to the relationship between CMPs' molecular structure and the photocatalytic activity of CMPs. Structural factors, such as the linker geometry, conjugation length, and molecular structure, play significant roles in regulating the charge transport and separation, energy band, and light adsorption of CMPs, thereby influencing the hydrogen production efficiency of CMP-based photocatalysts. Zhou et al. reported that the photocatalytic performance for H<sub>2</sub> evolution could be increased by including a secondary acceptor unit of the A<sub>1</sub>-A<sub>2</sub> type in the polymer chain. Nevertheless, because the acceptor units cannot transport electrons effectively, this photocatalyst series exhibits weak photocatalytic activity [54]. Meanwhile, the push-pull mechanism in donor-acceptor (D-A)-type copolymers may lower the bandgap of the polymer to boost solar energy harvesting and efficiently segregate photoinduced excitons, making them an extraordinary option for obtaining high photocatalytic hydrogen evolution efficiency. Yu et al. observed that developing a D-A polymer structure successfully enhanced the photocatalytic activity of CMPs [55]. Jiang et al. developed the donor-acceptor (D-A) polymer containing dibenzothiophene dioxide, demonstrating high photocatalytic performance due to the effective separation of light-induced charge carriers [52]. A twisted polyaromatic hydrocarbon called dibenzo[g,p]chrysene (TBN) has a structure consisting of two phenanthrenyl planes. TBN is well known for its superior thermal stability, ultraviolet–visible (UV–vis) absorption, bright fluorescence, and good carrier transport capacity owing to its stiff molecular structure and definite conjugation [56,57]. TBN derivatives also exhibit unique photophysical and electrical properties [58–60]. To the best of our knowledge, prior research has primarily focused on utilizing a TBN unit as a donor to increase visible light absorption, relying on the surface area. However, there has been no reported use of TBN as an acceptor to adjust the photophysical characteristics of polymers, for the purpose of

enhancing photocatalytic effectiveness. The implementation of a potent electron acceptor, such as benzo[c] [1,2,5]thiadiazole (BT), resulted in the extraction of electrons from the polymer, leading to the concentration of the active site solely on the BT moiety. This, in turn, minimized the active sites available on the polymer. Conversely, utilizing a feeble acceptor like TBN, which caused the electrons to distribute over both the TBN moiety and the triple bond, enabled the maximization of active sites on the polymer.

In this study, three types of TBN-based CMPs with different molecular structures were investigated for the first time and compared with respect to their energy storage and photocatalytic activity. To confirm and understand this effect, three monomers, dibenzo[g,p]chrysene (TBN), benzo[c] [1,2,5]thiadiazole (BT), and triphenylamine (TPA), were utilized to create three different kinds of TBN-based CMPs: TBN-TBN (D-D), TBN-TBN-TPA (A-D), and TBN-TBN-BT (D-A) via Sonogashira–Hagihara coupling reaction for energy storage and photocatalytic hydrogen evolution. The chemical structures, porosity, thermal stability, morphology, and crystallinity properties of the TBN-TBN, TBN-TBN-TPA, and TBN-TBN-BT CMPs are discussed in detail. Based on electrochemical results, the TBN-TBN-BT CMP sample demonstrated excellent capacity retention (98.2%) over 2000 cycles and high capacitor (130 F g<sup>-1</sup>) at 0.5 A g<sup>-1</sup>. The HER findings are in the following order 8452, 9800, and 3060  $\mu\text{mol g}^{-1} \text{h}^{-1}$  for TBN-TBN, TBN-TPA, and TBN-BT CMPs, respectively, according to photocatalytic measurement. The results of this study indicate that incorporating TBN as an acceptor leads to an increase in active sites for proton reduction, which effectively enhances the rate of H<sub>2</sub> evolution.

## 2. Experimental section

### 2.1. Materials

Triphenylamine (TPA, 98%), anhydrous ferric chloride (FeCl<sub>3</sub>, 99.9%), (trimethylsilyl)acetylene (TMSA, 98%), diethylamine, bromine solution (Br<sub>2</sub>), triphenylphosphine (PPh<sub>3</sub>, 99%), copper(I) iodide (CuI, 99%), benzophenone, *N*-bromosuccinimide (NBS, 99%), potassium carbonate (K<sub>2</sub>CO<sub>3</sub>, 99.9%), nitromethane (CH<sub>3</sub>NO<sub>2</sub>), acetic acid (AcOH), dichloromethane (DCM), benzophenone (99%), zinc (Zn, 98%), titanium tetrachloride (TiCl<sub>4</sub>, 99.9%), anhydrous Et<sub>3</sub>N (99%), [Pd(PPh<sub>3</sub>)<sub>4</sub>] and PdCl<sub>2</sub>(PPh<sub>3</sub>)<sub>2</sub> were ordered from Acros and Sigma–Aldrich. The synthesis of TPA-Br<sub>3</sub>, BT-Br<sub>2</sub>, TPE, TPE-Br<sub>4</sub>, and TBN-Br<sub>4</sub> were discussed and provided in the supporting information file [5,32,61–64, Figures S1–S15].

### 2.2. Synthesis of 2,7,10,15-tetrakis(trimethylsilyl)ethynyl)dibenzo[g,p]chrysene (TBN-TMS)

1.5 g of TBN-Br<sub>4</sub> (2.33 mmol) was dissolved in 125 mL of diethylamine. The solution was treated with a combination of PdCl<sub>2</sub>(PPh<sub>3</sub>)<sub>2</sub> (0.08 g), CuI (0.11 g), and TMSA (1.83 g, 18.63 mmol). The mixture was then stirred for 24 h at 80 °C. After the workup process, the yellow powder (1.3 g, 86%) was afforded after purification via silica gel column (DCM as eluent). FTIR (Figure S16): 3291 (C≡C–H), 3031 (aromatic C–H), 2957 (aliphatic C–H), 2156 (C≡C), and 1632 (C=C). <sup>1</sup>H NMR (Figure S17):  $\delta$  8.77, 8.47, 7.69, 0.34 (s, 36H, CH<sub>3</sub>). <sup>13</sup>C NMR (Figure S18): 131.24, 128.74, 121.90, 105.38, 96.34, 30.59, 3.5.

### 2.3. Synthesis of 2,7,10,15-tetraethynyl)dibenzo[g,p]chrysene (TBN-T)

TBN-TMS (1 g, 1.40 mmol) was mixed in MeOH (60 mL)/DCM (40 mL) before stirring for 24 h with 1.2 g of K<sub>2</sub>CO<sub>3</sub> (8.65 mmol). After the workup process using DCM/H<sub>2</sub>O, the TBN-T compound was obtained as an orange solid (0.8 g, 80%). FTIR (Figure S19): 3291 (C≡C–H), 3057 (aromatic C–H), 2106 (C≡C), and 1604 (C=C). <sup>1</sup>H NMR (Figure S20): 3.30 (s, 4H), 7.73 (s, 4H), 8.53 (s, 4H), 8.81 (s, 4H). <sup>13</sup>C NMR (Figure S21): 135.70, 132.40–101.60, 84.21, 78.87.

## 2.4. Synthesis of TBN-TBN-BT CMP

A solution containing BT-Br<sub>2</sub> (0.1 g, 0.34 mmol), TBN-T (0.1, 0.16 mmol), TBN-Br<sub>4</sub> (0.1 g, 0.24 mmol), Pd (0.03, 0.03 mmol), PPh<sub>3</sub> (0.01 g, 0.02 mmol), and CuI (0.01 g, 0.03 mmol) was heated in DMF (5 mL)/Et<sub>3</sub>N (5 mL) at 90 °C for 72 h to give a brown precipitate. FTIR: 3054 (aromatic C-H), 2204 (C≡C), 1603 (C=C).

## 2.5. Synthesis of TBN-TBN CMP

The TBN-TBN CMP was prepared using a similar approach to prepare TBN-TBN-BT CMP: TBN-T (0.1 g), TBN-Br<sub>4</sub> (0.1 g), Pd (0.03 g), PPh<sub>3</sub> (0.01 g), and CuI (0.01 g) to produce a yellow solid. FTIR: 2202 (C≡C), 1601 (C=C).

## 2.6. Synthesis of TBN-TBN-TPA CMP

The TBN-TBN-TPA CMP was prepared using a similar approach to prepare TBN-TBN-BT CMP: TPA-Br<sub>3</sub> (0.1 g), TBN-T (0.1 g), TBN-Br<sub>4</sub> (0.1 g), Pd (0.03 g), PPh<sub>3</sub> (0.01 g), and CuI (0.01 g) to get a yellow solid. FTIR: 1598 (C=C), 2202 (C≡C), 3057 (aromatic C-H).

## 3. Results and discussion

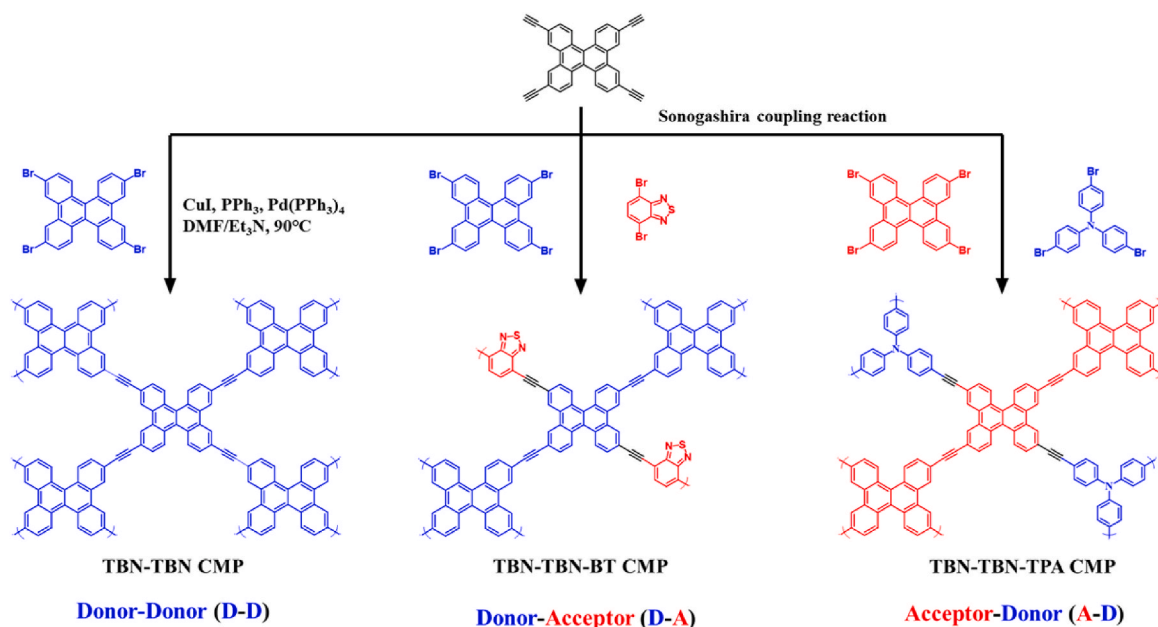
### 3.1. Synthesis and characterization of TBN-TBN-BT CMP, TBN-TBN CMP, and TBN-TBN-TPA CMP

The TBN-T monomer was prepared in three steps, as shown in the supporting file. First, TPE-Br<sub>4</sub> was reacted with anhydrous FeCl<sub>3</sub> in dry nitromethane and DCM to obtain TBN-Br<sub>4</sub> as a yellow powder. Next, the TBN-Br<sub>4</sub> precursor was reacted with (trimethylsilyl)acetylene (TMSA) in the presence of CuI in diethylamine as the solvent to obtain TBN-TMS as a yellow solid. Finally, TBN-T was successfully synthesized via the reaction of TBN-TMS with K<sub>2</sub>CO<sub>3</sub> in methanol and DCM to give a yellow solid. The peaks at 3291, 3057, 2106, and 1604 cm<sup>-1</sup> in the FTIR profile of TBN-T [Figure S19] were assigned to C≡C-H, aromatic C-H, C≡C, and C=C stretching, respectively. The <sup>1</sup>H NMR spectrum of TBN-T [Figure S20] shows the proton's signal at 3.30, 7.73, 8.53, and 8.81 ppm for C≡C-H and aromatic rings. In addition, the carbon peaks in the TBN-T compound appeared at 135.70-101.60, 84.21, and 78.87 ppm

due to the presence of aromatic rings and C≡C units in the molecular structure of TBN-T, as presented in the <sup>13</sup>C NMR spectrum [Figure S21]. The TBN-based CMPs were obtained through Sonogashira couplings between TBN-T as a building block and TBN-Br<sub>4</sub>/BT-Br<sub>2</sub>, TBN-Br<sub>4</sub>, and TBN-Br<sub>4</sub>/TPA-Br<sub>3</sub>, respectively, in the presence of a catalyst [Pd(PPh<sub>3</sub>)<sub>4</sub>] over 72 h (Scheme 1) to afford TBN-TBN-BT CMP as a brown solid, TBN-TBN CMP as a yellow powder, and TBN-TBN-TPA CMP as a yellow solid. The resulting TBN-based CMPs are insoluble in EtOH, DCM, THF, MeOH, DMSO, and acetone. The TBN-based CMP materials were investigated using FTIR and ssNMR to identify their chemical structures (Fig. 1(a)). The absorption bands at approximately 3058 and 1603 cm<sup>-1</sup> reveal the C-H aromatic and C=C units in the TBN-CMP frameworks, respectively [Fig. 1(b), S22, S23, and S24]. Furthermore, all TBN-CMPs had absorption bands for internal -C≡C- units around 2200 cm<sup>-1</sup>, demonstrating that TBN-TBN-BT, TBN-TBN, and TBN-TBN-TPA CMPs were effectively prepared through the Sonogashira reaction. The carbon atoms of the aromatic units were detected by <sup>13</sup>C ssNMR spectroscopy [Fig. 1(c)] in the ranges of 130.1–116.4 ppm for TBN-TBN-BT CMP, 140.7–120.3 ppm for TBN-TBN CMP, and 142.8–121.3 ppm for TBN-TBN-TPA CMP. Additionally, it was discovered that the carbon signals of the internal -C≡C- units of the TBN-TBN-BT, TBN-TBN, and TBN-TBN-TPA CMPs were 81.7, 80.3, and 80.2 ppm, respectively. Thermogravimetric analysis (TGA) indicated that the three prepared TBN-CMPs had good thermal stability, and the 10% weight loss of TBN-TBN-BT, TBN-TBN, and TBN-TBN-TPA CMPs occurred at 388, 386, and 382 °C under N<sub>2</sub>, with char yields of 67, 63, and 62 wt%, respectively [Fig. 1(d)].

To further explore the synthesis of TBN-CMPs, X-ray photoelectron spectroscopy (XPS) was used to analyze the compositions of surfaces of the TBN-TBN-BT, TBN-TBN, and TBN-TBN-TPA CMPs (Fig. 2). The XPS survey spectra of the TBN-based CMPs indicate the presence of C in TBN-TBN CMP, C, and N in TBN-TBN-TPA CMP, and C, N, and S in TBN-TBN-BT CMP (Fig. 2(a)), as expected. Fig. 2(b) shows high-resolution XPS spectra of N1s and S2p. Where TBN-TBN-TPA and TBN-TBN-BT CMPs showed a main peak in the N1 s spectra at 398.26 and 398.91 eV for TBN-TBN-TPA and TBN-TBN-BT CMPs, respectively. In addition, TBN-TBN-BT CMP showed an additional peak for sulfur in the BT unit in S2p at 164.34 eV (Fig. 2(c)).

The specific surface areas and porosities of the three TBN-based CMPs were determined based on the adsorption/desorption behavior



Scheme 1. Schematic approach for the synthesis of TBN-TBN-BT, TBN-TBN and TBN-TBN-TPA CMPs.

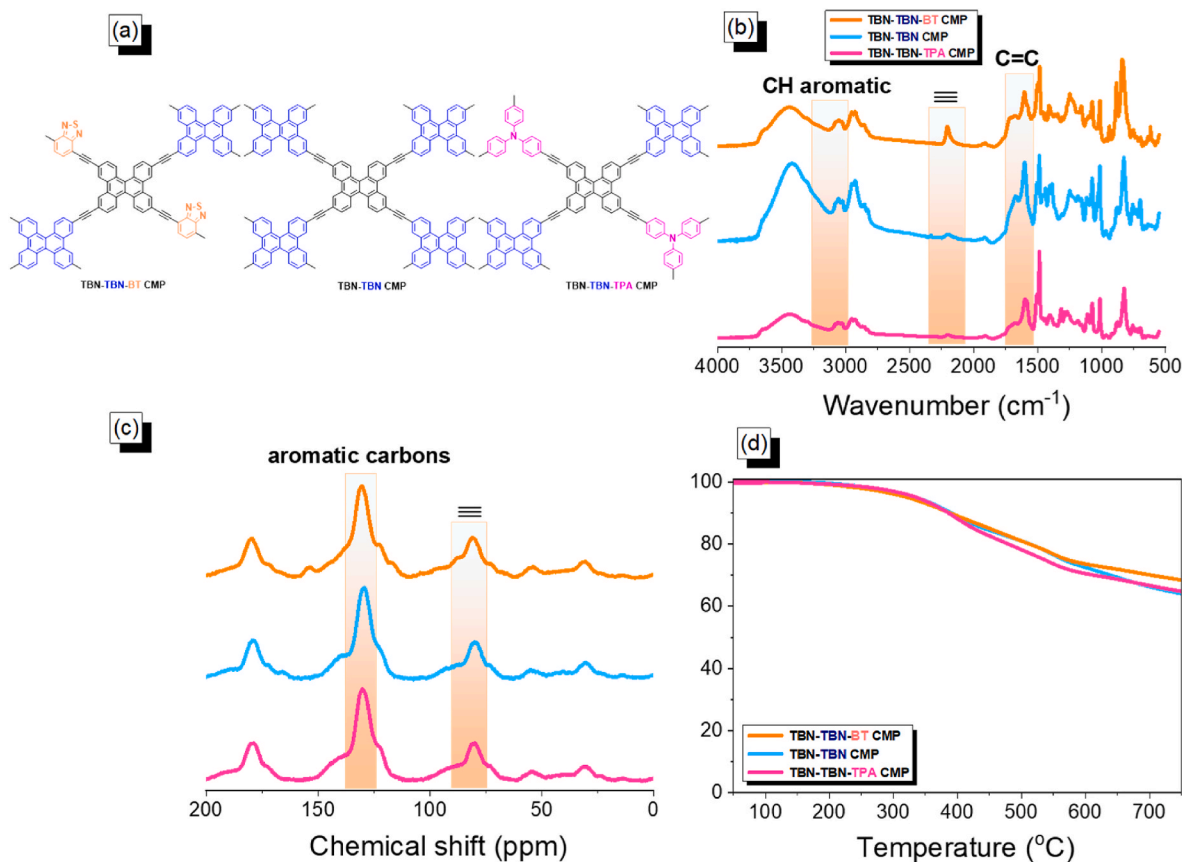


Fig. 1. (a) Molecular structures, (b) FTIR, (c) solid state  $^{13}\text{C}$  NMR, and (d) TGA curves of TBN-TBN-BT, TBN-TBN, and TBN-TBN-TPA CMPs.

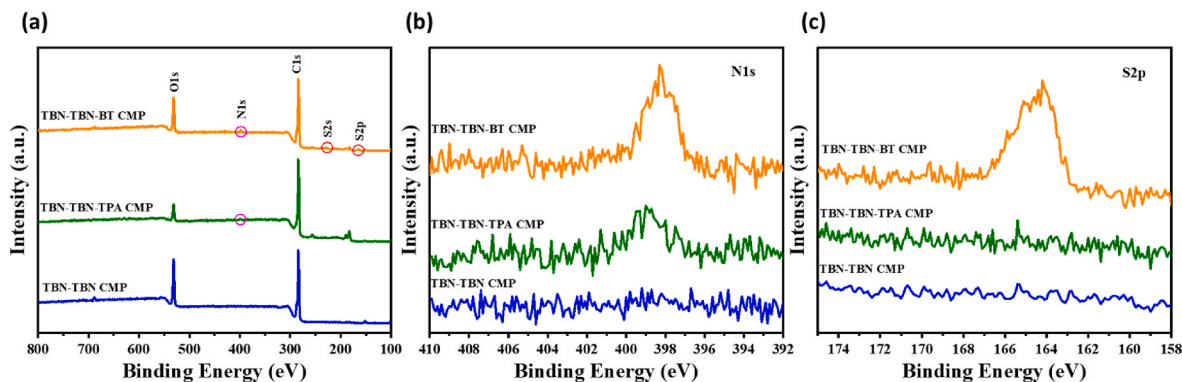


Fig. 2. (a) Survey XPS spectra of the TBN-TBN-BT, TBN-TBN, and TBN-TBN-TPA CMPs and high-resolution XPS of (b) N1s and (c) S2p.

of  $\text{N}_2$  at 77 K. As illustrated in Fig. 3(a–c), the three TBN-CMP samples exhibited a type-II isotherm with an H1 hysteresis loop that surged in the lower  $P/P_0$  region ( $<0.02$ ), confirming that these materials have a large number of micropores. The specific surface areas of TBN-TBN-BT CMP, TBN-TBN CMP, and TBN-TBN-TPA CMP were 217, 488, and 442  $\text{m}^2 \text{g}^{-1}$ , respectively, and their corresponding total pore volumes were 0.36, 0.40, and 0.63  $\text{cm}^3 \text{g}^{-1}$  respectively. In addition, we estimated the pore size curves of the three TBN-CMPs [Fig. 3(d–f)] using nonlocal density functional theory (NLDFT). The pore size exposes that TBN-TBN and TBN-TBN-TPA CMPs have two sizes of micropores (average diameter: 0.44, 1.80 nm and 1.20, 1.96 nm, respectively), while TBN-TBN-BT CMP has mesopores with an average diameter of about 2.24 nm (Fig. 3(d–f)). The TBN-CMPs with amorphous structures were reflected in the X-ray diffraction pattern [Figure S25], which did not show any crystalline diffraction peaks, similar to other reported CMPs networks.

The surface morphologies of TBN-TBN-BT CMP, TBN-TBN CMP, and TBN-TBN-TPA CMP were visualized by scanning electron microscopy (FE-SEM). The morphologies of TBN-TBN-BT CMP and TBN-TBN CMP were regular small spherical structures, and TBN-TBN-TPA CMP displayed regular large spherical nanoparticles [Fig. 4(a–c)]. Furthermore, the elemental composition of these TBN-CMPs was investigated using energy-dispersive X-ray spectroscopy (EDS), as illustrated in Figs. S26–S28. The data revealed that the elements C, N, and S in TBN-TBN-BT CMP were distributed with a weight content of 61.56% for C atoms, 37.49% for N atoms, and 0.94% for S atoms [Figure S26]. The weight content of C atoms in the TBN-TBN CMP framework was 100% [Figure S27]. The C and N elements were mostly supplied in TBN-TBN-TPA CMP, and the contents of C and N were 55.89 and 44.11%, respectively, in the TBN-TBN-TPA CMP framework [Figure S28]. Additionally, the TEM images (Fig. 4(d–f)) confirmed the shape of the TBN-

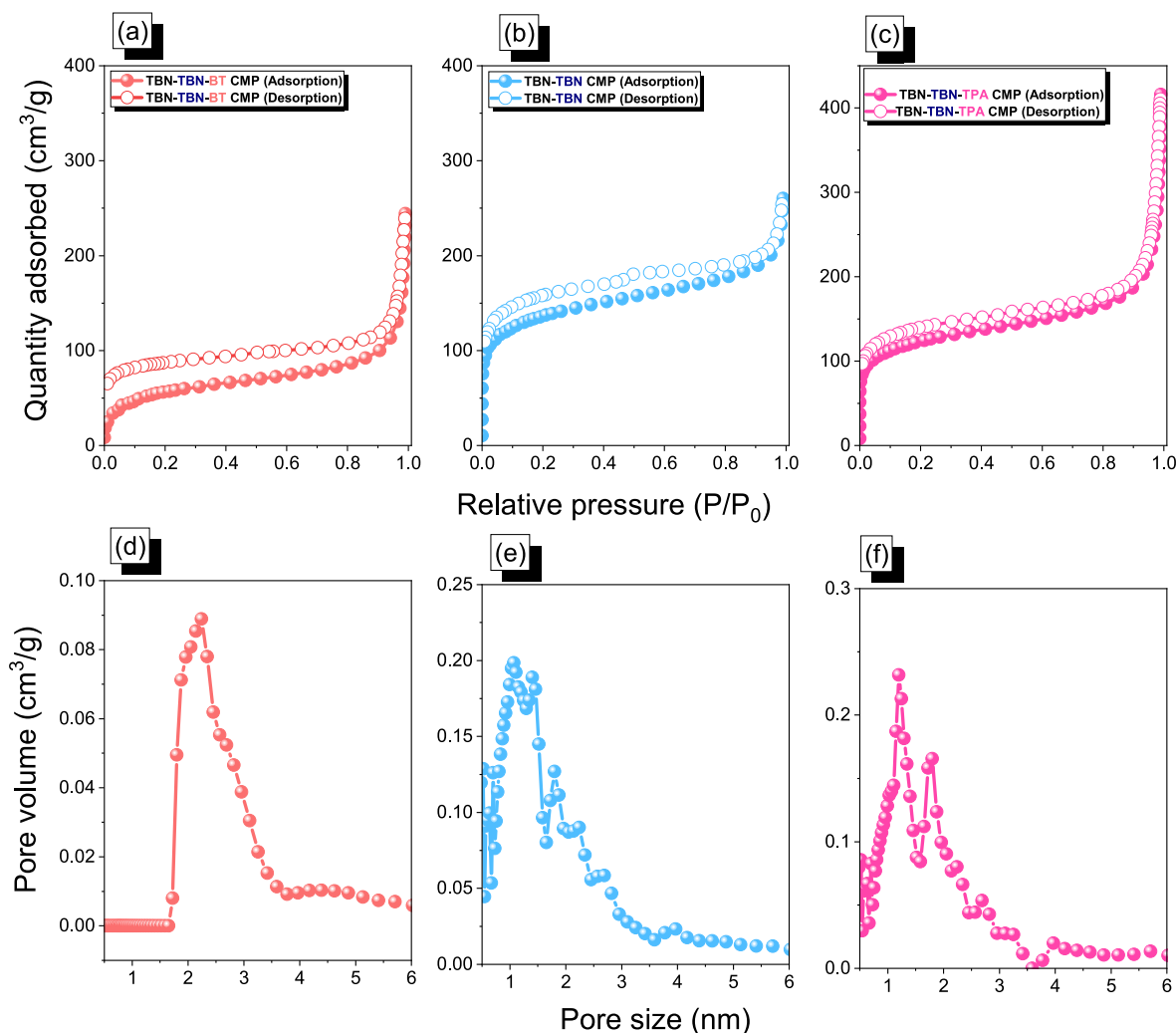


Fig. 3. (a–c) BET isotherms and (d–f) pore size diagrams of TBN-TBN-BT CMP (a, d), TBN-TBN CMP (b, e) and TBN-TBN-TPA CMP (c, f).

CMPs. These images demonstrate the amorphous properties of TBN-TBN-BT, TBN-TBN, and TBN-TBN-TPA CMPs, as well as tiny holes that indicate a porous structure.

### 3.2. Electrochemical performance of TBN-TBN-BT, TBN-TBN, and TBN-TBN-TPA CMPs

To compare the electrochemical performance, we measured the behavior of all TBN-based CMPs in a three-electrode system using cyclic voltammetry (CV) and galvanostatic charge-discharge (GCD) using a 1 M KOH aqueous solution as the electrolyte. Fig. 5(a–c) show the CV profiles of the TBN-CMP materials at various scan rates ( $5\text{--}200\text{ mV s}^{-1}$ ). The rectangular shapes exhibited in the CV curves of all TBN-based CMPs indicate that they originate from the capacitive response of electric double-layer capacitance (EDLC). The rectangle of TBN-TBN-TPA CMP has the appearance of an extra bulge, which is the reversible radical redox behavior of the pseudo-capacitor during the charging and discharging processes [5]. As the scan rate increased from 5 to  $200\text{ mV s}^{-1}$ , the current density was enhanced, and the maintenance of the CV curve demonstrated its excellent rate capability. Moreover, the GCD measurements in Fig. 5(d–f) are all detected from  $0.5\text{ to }20\text{ A g}^{-1}$  and display a slightly curved triangular shape, which is a pseudocapacitor and EDLC characterization.

From the GCD curves, the estimated specific capacitance values of the TBN-TBN, TBN-TBN-TPA, and TBN-TBN-BT CMPs were 108, 95, and  $130\text{ F g}^{-1}$  at a  $0.5\text{ A g}^{-1}$ , respectively, as depicted in Fig. 6(a). The

specific capacitances of three electrode materials, TBN-TBN, TBN-TBN-TPA, and TBN-TBN-BT CMP, are summarized in Table S1 along with other porous electrode precursors. The stability graphs (Fig. 6(b–d)) of the TBN-based CMPs were measured for 2000 cycles at  $10\text{ A g}^{-1}$ . TBN-TBN-BT-CMP had the best capacitance retention rate of 98.2% compared to TBN-TBN CMP (85.7%) and TBN-TBN-TPA CMP (95.5%).

### 3.3. Photocatalytic performance of TBN-TBN-BT CMP, TBN-TBN CMP, and TBN-TBN-TPA CMP for $\text{H}_2$ production

Next, the synthesized TBN-TBN, TBN-TBN-TPA, and TBN-TBN-BT CMPs were examined through photocatalytic  $\text{H}_2$  production measurements. UV/visible absorption spectra were measured for all the polymers in methanol to investigate their photophysical properties, as shown in Fig. 7(a). As expected, the TBN-TBN-TPA and TBN-TBN-BT CMPs have the most red-shifted absorption onset compared to TBN-TBN CMP, which is a result of the addition of TPA and BT in the TBN-TBN-TPA and TBN-TBN-BT CMPs, respectively. As the acceptor strength increased, the absorption spectrum was slightly red-shifted. The estimated optical bandgap ( $E_g$ ) of TBN-TBN, TBN-TBN-TPA, and TBN-TBN-BT CMPs is 1.98, 2.0, and 1.75 eV, respectively based on Tauc plots [Fig. 7(b)], considering the light absorption, which is suitable for photocatalytic water splitting process. As shown in Fig. 7(c) and Table 1, the energy levels of the HOMOs for TBN-TBN, TBN-TBN-TPA, and TBN-TBN-BT CMPs were determined using ultraviolet photoelectron spectroscopy (UPS). The LUMO energy levels of the TBN-TBN, TBN-TBN-TPA, and

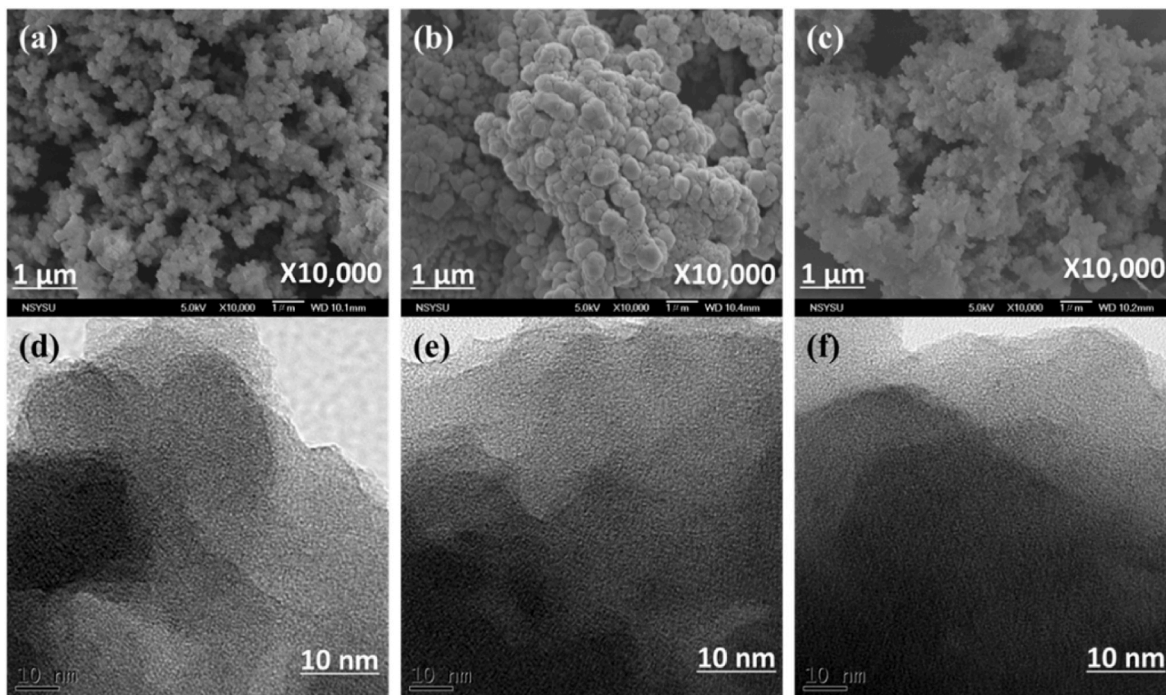


Fig. 4. (a–c) SEM and (d–f) TEM images of TBN-TBN-BT CMP (a, d), TBN-TBN CMP (b, e), and TBN-TBN-TPA CMP (c, f).

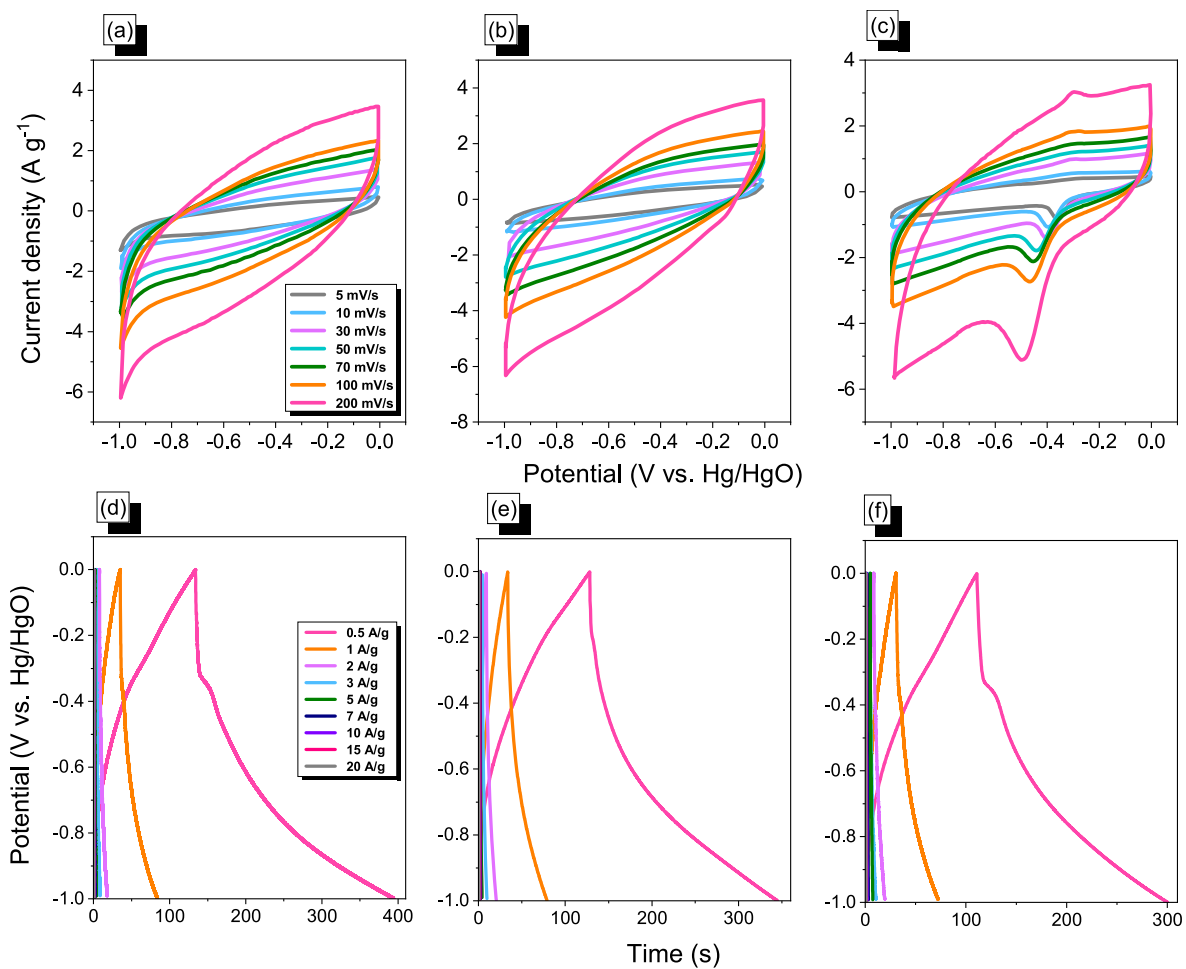


Fig. 5. (a–c) CV and (d–f) GCD curves of TBN-TBN-BT CMP (a, d), TBN-TBN CMP (b, e) and TBN-TBN-TPA CMP (c, f).

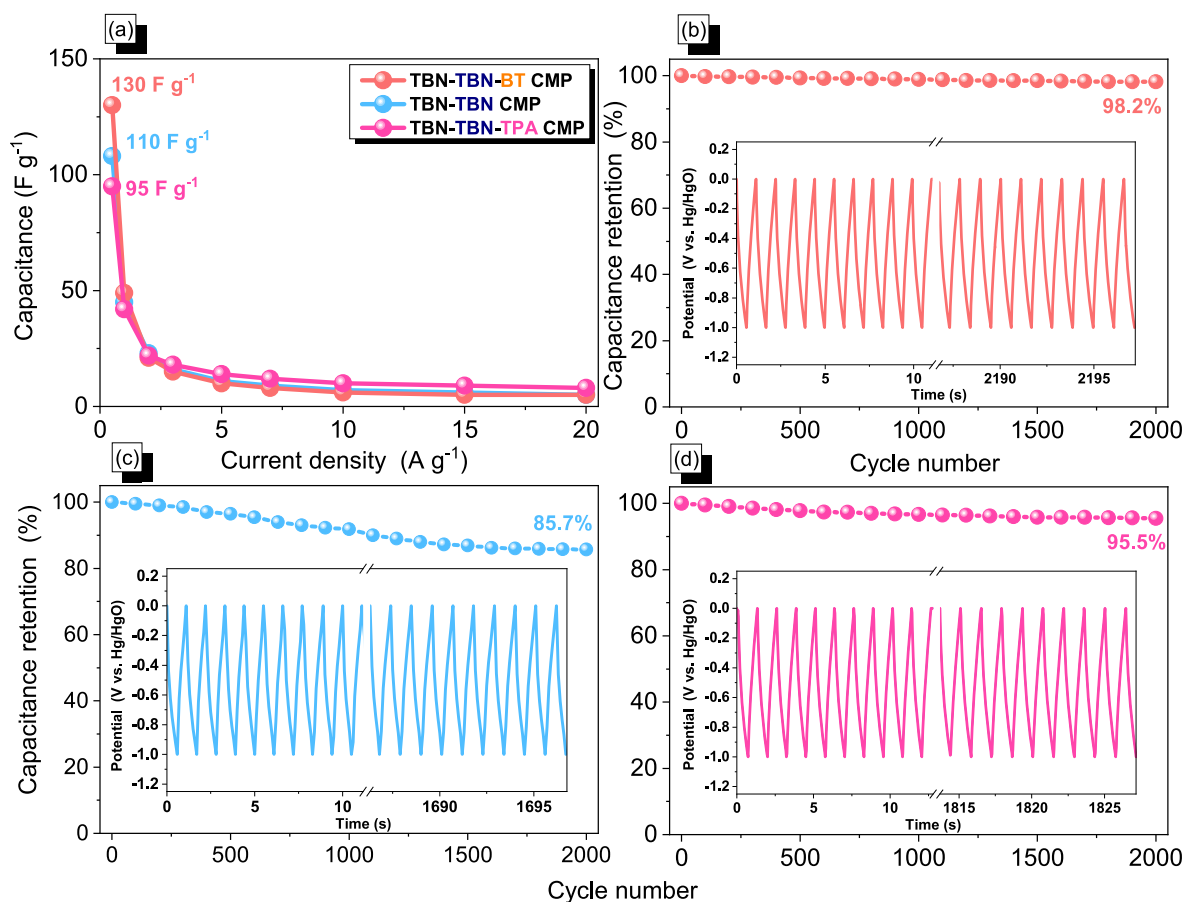


Fig. 6. (a) Capacitances of TBN-TBN-BT, TBN-TBN and TBN-TBN-TPA CMPs and cycling stabilities of TBN-TBN-BT (b), TBN-TBN (c) and TBN-TBN-TPA CMPs (d).

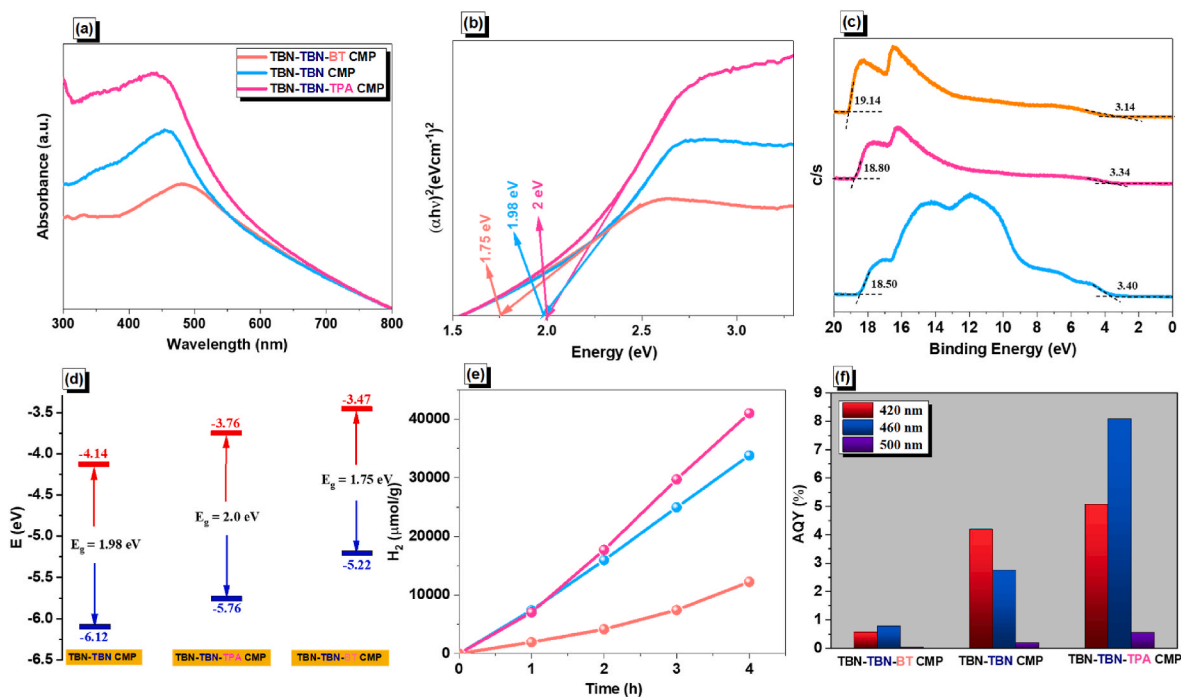


Fig. 7. (a) UV-vis absorption spectra of the TBN-based CMPs, (b) the corresponding Tauc of TBN-based CMPs, (c) valence band UPS cutoff spectra. (d) Energy level diagram of the TBN-based CMPs photocatalysts, (e) hydrogen evolution under visible-light irradiation ( $\lambda$ : 380–780 nm) using TBN-based CMPs, and (f) AQYs of the TBN-based CMPs at various wavelengths of light.

**Table 1**  
Photophysical properties and HER of the TBN-CMPs.

| Polymer         | HOMO/<br>LUMO (eV) | Bandgap<br>(eV) | HER ( $\mu\text{mol g}^{-1} \text{h}^{-1}$ ) | AQY (%)   |           |           |
|-----------------|--------------------|-----------------|--|-----------|-----------|-----------|
|                 |                    |                 |  | 420<br>nm | 460<br>nm | 500<br>nm |
| TBN-TBN         | -6.12/<br>4.14     | 1.98            | 8452   | 4.19      | 2.74      | 0.19      |
| TBN-TBN-<br>TPA | -5.76/<br>3.76     | 2.00            | 9800   | 5.07      | 8.10      | 0.56      |
| TBN-TBN-<br>BT  | -5.22/<br>3.47     | 1.75            | 3060   | 0.57      | 0.79      | 0.03      |

TBN-TBN-BT CMPs are  $-4.14$ ,  $-3.76$ , and  $-3.47$  eV [Fig. 7(d)], demonstrating that they may all have been stimulated to generate  $\text{H}_2$  by visible light. Studies on photocatalytic hydrogen evolution have been carried out at room temperature under visible-light irradiation (380–780 nm). Gas chromatography (GC) was used to measure the gas generated in the photoreactor (500  $\mu\text{L}$ ) for 1 h. During the investigation of photocatalytic  $\text{H}_2$  evolution from water, methanol was added to the three TBN-CMPs in the presence of ascorbic (AA) as a sacrificial electron donor (SED) to increase the dispersing of the photocatalysts in water. The platinum (Pt) co-catalyst was produced in situ by adding  $\text{H}_2\text{PtCl}_6$ , which enhanced photocatalytic  $\text{H}_2$  evolution. First, we examined TEA, TEOA, and AA as sacrificial donors and Pt cocatalysts in aqueous solutions of TBN-TBN, TBN-TBN-TPA, and TBN-TBN-BT CMPs by monitoring the HER for 4 h while exposed to visible light (Figure S29). The HER of the photocatalytic process is greatest when AA is employed as the SED. Therefore, ascorbic acid was employed to perform further optimization testing, as mentioned in the supplementary information (Figure S30). The amount of AA serving as an electron donor source was then tuned using three concentrations (0.05, 0.1, and 0.2 M) (Figure S30). With 0.2 M of AA, the HER performance of the TBN-TBN and TBN-TBN-TPA CMPs was good. When utilizing 0.1 M of AA, the TBN-TBN-BT CMP demonstrated the most efficient photocatalytic  $\text{H}_2$  evolution. Next, we examined the effects of various Pt co-catalyst contents utilizing the ideal experimental conditions for the TBN-CMPs for  $\text{H}_2$  evolution (the origin of Pt was  $\text{H}_2\text{PtCl}_6$ :2–6 wt%) (Figure S31). Surprisingly, adding 2 wt% Pt noble metal to the TBN-CMPs solution as a co-catalyst resulted in an outstanding HER. We also examined the impact of the three synthetic TBN-CMPs at different doses (1.0, 2.0, and 3.0 mg) on HERs (Figure S32). The mass of the polymers has an inverse relationship with the photocatalytic activity. The amount of  $\text{H}_2$  produced per unit of irradiation area is the most important factor in photocatalysis. The polymers operated best at 1 mg (Figure S32). Because of

the poor light transmission and inadequate use of high polymer concentrations, the HER decreased as the amount of polymer increased. As shown in Fig. 7(e), TBN-TBN-TPA CMP has the highest photocatalytic hydrogen evolution (HER) approximately  $9800 \mu\text{mol g}^{-1} \text{h}^{-1}$ , demonstrating the potential of the A-D method for developing highly effective polymer photocatalysts. Using three distinct bandpass filters at 420, 460, and 500 nm, to determine how much the spectrum contributed to the  $\text{H}_2$  production ability of the TBN-CMPs photocatalysts, the apparent quantum yield (AQY) was computed, as shown in Fig. 7(f). The AQY obtained for TBN-TBN-TPA CMP was 8.09% at an incident light wavelength of 460 nm. Photocatalytic processes depend on separating photoinduced holes and electrons and their mobility.

The PL spectra of the TBN-TBN, TBN-TBN-TPA, and TBN-TBN-BT CMPs were measured in methanol, as shown in Fig. 8(a). Compared with that of TBN-TBN CMP, the FL intensity of the TBN-TBN-TPA and TBN-TBN-BT CMPs decreased significantly. TBN-TBN-TPA CMP has the lowest fluorescence intensity, demonstrating that it has the greatest capacity to separate photogenerated electrons from holes, which is advantageous for its  $\text{H}_2$  performance. Furthermore, electrochemical impedance spectroscopy was used to study the electric resistance offered by various electrodes via the ion diffusion process. Several Nyquist plots with similar fitted circuits are shown in Fig. 8(b) and Figure S33 allowing us to identify several characteristics of the electrodes, such as their circuit series-resistance and charge transfer resistances across the interface, constant-phase-element, capacitance phase element of the semiconductor-electrolyte interface, and the Warburg element, which are all represented in the fitting circuit as  $R_s$ ,  $R_{ct}$ , CPE, C, and  $Z_w$ , respectively [Figure S33]. According to Table S2, the electrodes of the TBN-TBN, TBN-TPA CMP and TBN-BT CMPs offered very similar initial series resistances of 8.30, 10.0, and 7.58  $\Omega$ , respectively. In addition to this, the charge transfer resistances offered by these three different electrodes namely TBN-TBN, TBN-TBN-TPA CMP, and TBN-TBN-BT CMPs were quite different. TBN-TBN CMP has offered the lowest charge transfer (263 m $\Omega$ ) followed by TBN-TBN-BT CMP (619 m $\Omega$ ) and TBN-TBN-TPA CMP (642 m $\Omega$ ). The photocatalytic  $\text{H}_2$  evolution findings are supported by the fact that the TBN-TBN-TPA CMP has the lowest resistance compared to the others (Fig. 8(b)), suggesting that it has better interfacial charge mobility than the others.

The control photocatalytic studies revealed, as shown in Fig. S34, that the  $\text{H}_2$  production could not be seen in pure  $\text{H}_2\text{O}$  in the absence of AA or TBN-CMP photocatalysts, demonstrating that the sacrificial agent and polymer photocatalysts are necessary for the photocatalytic evolution of hydrogen. One of the factors used to gauge the potential of TBN-TBN, TBN-TBN-TPA, and TBN-TBN-BT CMPs as photocatalysts for

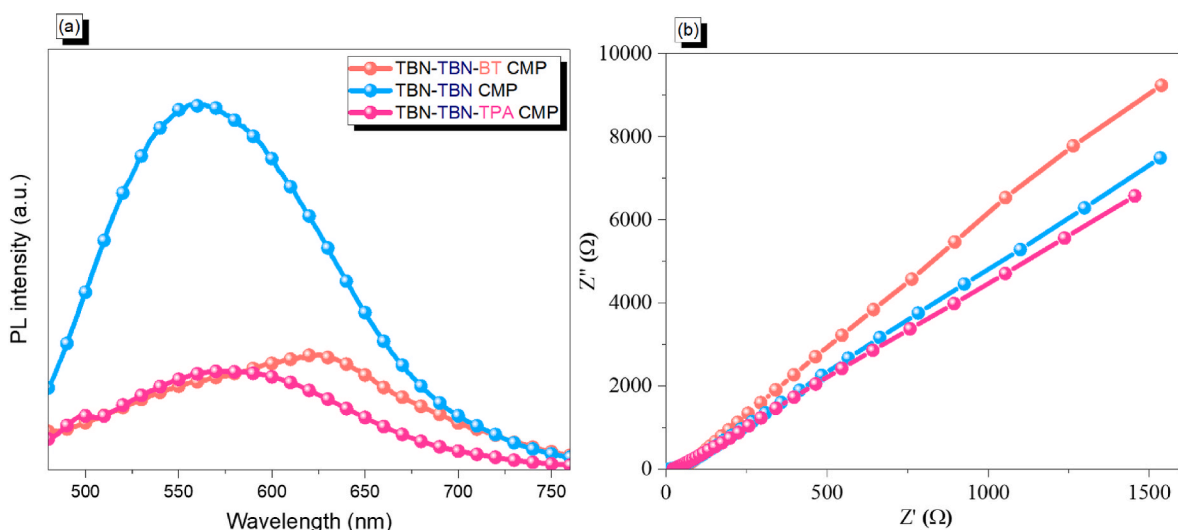


**Fig. 8.** (a) PL and (b) Nyquist curves of TBN-based CMPs.

hydrogen evolution is their stability. After prolonged irradiation, all TBN-CMPs exhibited almost unaltered FTIR absorption bands for aromatic CH ( $\sim 3044\text{ cm}^{-1}$ ) and alkynyl groups ( $\sim 2200\text{ cm}^{-1}$ ) in their framework structures [Figures S35-S37].

To clarify the structure-property relationship of TBN-TBN, TBN-TBN-TPA, and TBN-TBN-BT CMPs and their HOMO/LUMO separations, DFT results were calculated at the B3LYP level using the 6-31G (d,p) basis set (Fig. 9, S38, S39, and S40). According to the findings of the theoretical calculation, TBN-TBN CMP is a donor-donor (D-D) system; as shown in Fig. 9, the TBN unit acts as an electron donor, where both HOMO and LUMO are distributed on the TBN groups. In the case of TBN-TBN-TPA CMP is an acceptor-donor (A-D) system, where the LUMO is mainly localized on TBN, and the HOMO is localized on the TPA groups. TBN-TBN-BT CMP is a donor-acceptor (D-A) system, where TBN acts as an electron donor, and BT acts as an electron acceptor (Fig. 9). These findings illustrate that A-D conjugation can effectively extend HOMO level delocalization, thus enabling inter- and intramolecular charge transfer and assuring high mobility [65].

Based on Fig. 10(a-c), we further investigated the charges on each atom of the TBN-TBN, TBN-TBN-TPA, and TBN-TBN-BT CMPs. The red color represents excess negative charges, while the green color represents excess positive charges, according to Mulliken population analysis [66]. In other words, the molecular charge at the surface of these CMPs is more negative (or more positive) when the sum of the charges is applied. The TBN-TBN module does not contain any heteroatoms, so the carbons on the TBN rings with non-fused carbons had the most negative charge ( $-0.238$ ), while the other fused carbon had the most positive charge. TBN-TBN-TPA CMP had the most negative charge of  $-0.653$  for nitrogen atoms in the triphenylamine moieties and the most positive charge values for carbon atoms that are directly connected to nitrogen atoms. Furthermore, The TBN-TBN-BT model compound contained more positive charges on the side ring of BT moiety, including sulfur and two fused carbons, than on the other side. A significant negative charge,  $-0.569$ , was exhibited by nitrogen and carbon on the BT rings. The most likely interactions of the active sites on the surface of the CMPs with the hydrogen protons on the reaction mixture during the photocatalytic activity were identified using electrostatic potential (ESP) contour mapping. To determine the system's reactivity, ESP can predict the electrophilic and nucleophilic sites in the target molecules. As noted in the ESP, the positive regions are associated with nucleophilic sites, whereas the negative areas are related to electrophilic sites. The

potential increase in the order of red < orange < yellow < green < blue. The ESP surfaces for the TBN-TBN, TBN-TBN-TPA and TBN-TBN-BT CMPs were calculated using the B3LYP level and 6-31G(d) basis set, as shown in Fig. 10(e-f). The carbon skeleton of TBN-TBN and TBN-TBN-TPA CMPs exhibit a significant negative potential spread, particularly around the triple bond of the carbon atoms. This is noteworthy because triple bonds are highly polarizable and can generate areas of high electron density, which can impact the material's overall electronic properties [67,68]. The electron density EPS mapping of CMPs that contain triple bonds can detect areas with high electron density surrounding the triple bonds, which can affect the material's electronic conductivity and reactivity. This can create more active sites for the reduction of water molecules to hydrogen ( $\text{H}_2$ ) during the photocatalytic reaction, as illustrated in Fig. 10(d) and (e). TBN-TBN-BT CMP demonstrates a highly negative potential around the N atoms, while the BT linker proton exhibits the highest positive potential (Fig. 10(f)). These results are consistent with the experimental photocatalytic activity of the TBN-based CMPs, as presented in Table 1. Table S3 presents a comparison of the synthesized TBN-TBN-BT, TBN-TBN, and TBN-TBN-TPA CMPs with other reported CMPs in terms of their photocatalytic hydrogen evolution performance.

### 3.4. The mechanistic study of TBN-based CMPs

ESP mapping is a valuable tool to investigate the interactions between CMPs and other molecules, such as solvents or guest molecules, which can provide useful insights into the material's potential applications in areas such as energy storage, gas separation, and catalysis [69]. Based on this approach, the proposed photocatalytic mechanism, depicted in Fig. 11, involves the A-D copolymer (TBN-TBN-TPA CMP), containing a triple bond as an active site that adsorbs water molecules from the reaction mixture and splits them into protons during photocatalysis. The absorption of photons generates electron/hole pairs. The polymer structure consists of two different types of acceptor moieties (TBN and triple bond), which facilitate and promote the transfer of light-induced electrons from TPA to the proton. The presence of a triple bond enhances the coplanarity of the polymer skeleton and leads to the transfer of excited electrons to the Pt co-catalyst surface, resulting in high proton reduction and hydrogen generation efficiency. Furthermore, AA molecules adsorb on the copolymer surface and capture light-induced holes from the HOMO orbits of the donor, producing

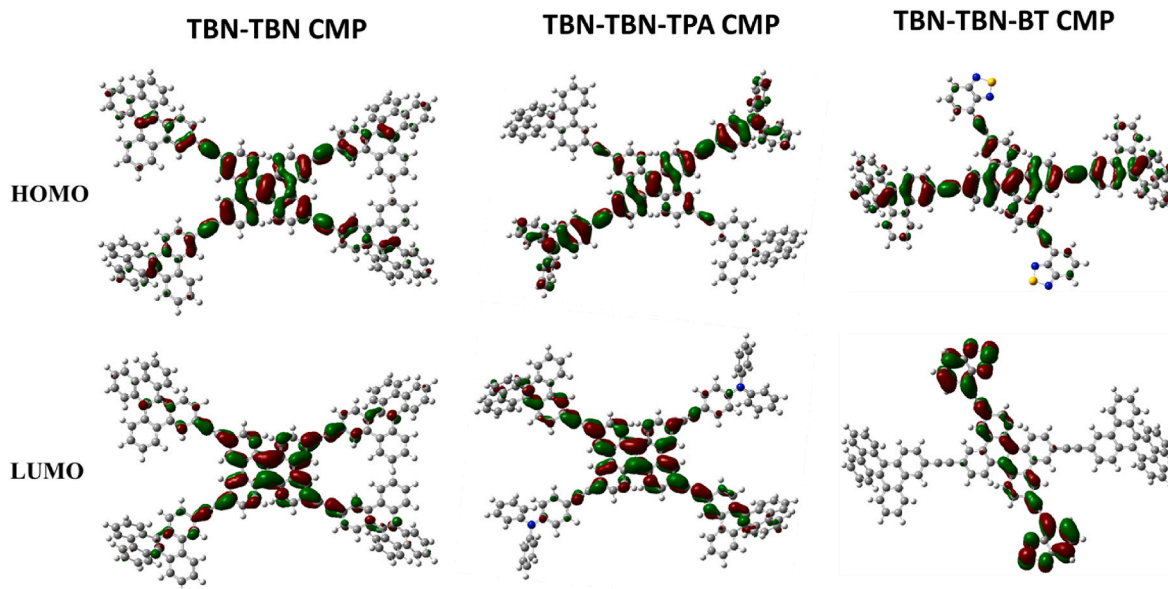


Fig. 9. Electron orbital distributions of the molecular orbitals of TBN-based CMPs.

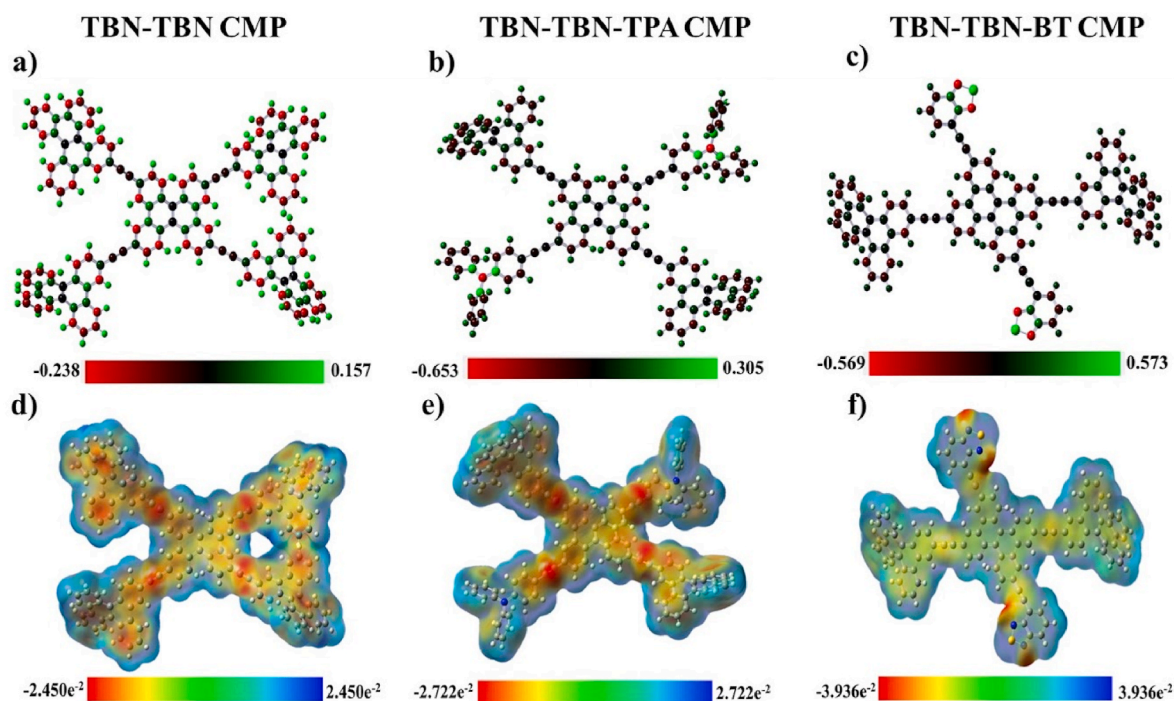


Fig. 10. (a–c) Mulliken charge and (d–f) electrostatic potential distributions for the TBN-based CMPs.

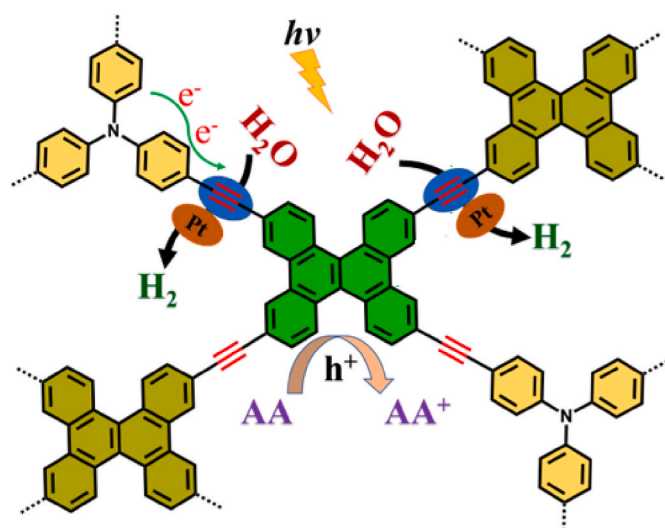


Fig. 11. The proposed photocatalytic mechanism of the TBN-TBN-TPA CMP photocatalyst.

oxidized AA. This mechanism promotes the photocatalytic hydrogen evolution reaction.

#### 4. Conclusion

A series of TBN-CMPs using three different systems, donor-donor (D-D), acceptor-donor (A-D), and donor-acceptor (D-A), were constructed via the Sonogashira reaction. The  $T_{d10}$  values of the TBN-TBN-BT, TBN-TBN, and TBN-TBN-TPA CMPs were 388, 383, and 382 °C, respectively, indicating that the synthesized TBN-CMPs possessed good thermal stability (based on the TGA data). According to the energy storage results, the capacitances of the TBN-TBN-BT, TBN-TBN, and TBN-TBN-TPA CMPs were 130, 110, and 95  $F g^{-1}$ , respectively. TBN-TBN-TPA CMP has the highest HER of approximately  $9800 \mu mol g^{-1} h^{-1}$ ,

demonstrating the potential of the A-D method for developing highly effective polymer photocatalysts. These results indicate that using TBN as an acceptor enhances the  $H_2$  evolution rate by increasing the number of active sites for hydrogen reduction. The obtained AQY for TBN-TBN-TPA CMP is 8.09% at incident light wavelengths of 460 nm. This study introduces an innovative approach to enhance the photocatalytic efficiency of conjugated polymer materials and their compatibility with various solar energy conversion technologies. The findings may offer a promising new method for developing such materials.

#### Credit authors statement

Siang-Yi Chang: Investigation, Methodology. Ahmed M. Elewa: Investigation, Methodology, Writing – original draft. Mohamed Gamal Mohamed: Investigation, Methodology, Conceptualization, Supervision, Writing – original draft. Islam M. A. Mekhmer: Investigation, Methodology, Writing – original draft. Maha Mohamed Samy: Investigation. Kan Zhang: Investigation, Methodology. Ho-Hsiu Chou: Supervision. Shiao-Wei Kuo: Supervision.

#### Declaration of competing interest

The authors declare that they have no known competing financial interests or personal relationships that could have appeared to influence the work reported in this paper.

#### Data availability

The data that has been used is confidential.

#### Acknowledgments

This study was supported financially by the Ministry of Science and Technology, Taiwan, under contracts NSTC 110-2124-M-002-013, NSTC 111-2223-E-110-004, NSTC 111-2628-E-007-009, NSTC 111-2221-E-007-004 and NSTC 111-2622-8-007-011. The authors thank the staff at National Sun Yat-sen University for their assistance with the TEM (ID:

EM022600) experiments.

## Appendix A. Supplementary data

Supplementary data to this article can be found online at <https://doi.org/10.1016/j.mtchem.2023.101680>.

## References

- [1] M. Kim, C. Wang, J. Earnshaw, T. Park, N. Amirilian, A. Ashok, J. Na, M. Han, A. E. Rowan, J. Li, J.W. Yi, Y. Yamauchi, Co, Fe and N co-doped 1D assembly of hollow carbon nanoboxes for high-performance supercapacitors, *J. Mater. Chem.* 10 (2022) 24056–24063, <https://doi.org/10.1039/D2TA06950D>.
- [2] M.G. Mohamed, M.H. Elsayed, Y. Ye, M.M. Samy, A.E. Hassan, T.H. Mansour, Z. Wen, H.H. Chou, K.H. Chen, S.W. Kuo, Construction of porous organic/inorganic hybrid polymers based on polyhedral oligomeric silsesquioxane for energy storage and hydrogen production from water, *Polymers* 15 (2023) 182, <https://doi.org/10.3390/polym15010182>.
- [3] A.O. Mousa, M.G. Mohamed, C.H. Chuang, S.W. Kuo, Carbonized aminal-linked porous organic polymers containing pyrene and triazine units for gas uptake and energy storage, *Polymers* 15 (2023) 1891, <https://doi.org/10.3390/polym15081891>.
- [4] M.G. Mohamed, S.Y. Chang, M. Ejaz, M.M. Samy, A.O. Mousa, S.W. Kuo, Design and synthesis of bisulfone-linked two-dimensional conjugated microporous polymers for CO<sub>2</sub> adsorption and energy storage, *Molecules* 28 (2023) 3234, <https://doi.org/10.3390/molecules28073234>.
- [5] M.M. Samy, M.G. Mohamed, S.U. Sharma, S.V. Chaganti, T.H. Mansour, J.T. Lee, T. Chen, S.W. Kuo, Constructing conjugated microporous polymers containing triphenylamine moieties for high-performance capacitive energy storage, *Polymer* 264 (2023), 125541, <https://doi.org/10.1016/j.polymer.2022.125541>.
- [6] M.M. Samy, M.G. Mohamed, S.W. Kuo, Pyrene-functionalized tetraphenylethylene polybenzoxazine for dispersing single-walled carbon nanotubes and energy storage, *Compos. Sci. Technol.* 199 (2020), 108360, <https://doi.org/10.1016/j.compscitech.2020.108360>.
- [7] C. Yang, C. Qian, M. Yu, Y. Liao, Manipulation of band gap and hydrophilicity in vinylene-linked covalent organic frameworks for improved visible-light-driven hydrogen evolution by end-capping strategy, *J. Chem. Eng.* 454 (2023), 140341, <https://doi.org/10.1016/j.ccej.2022.140341>.
- [8] Z. Ajmal, A. Qadeer, U. Khan, M.B. Hussain, M. Irfan, M. Abid, R. Djellabi, A. Kumar, H. Ali, A. Kalam, H. Algarni, Y. Al-Hadeethi, J. Qian, A. Hayat, H. Zeng, Current progresses in two-dimensional MXene-based framework: prospects from superficial synthesis to energy conversion and storage applications, *Mater. Today Chem* 27 (2023), 101238, <https://doi.org/10.1016/j.mtchem.2022.101238>.
- [9] M.M. Samy, I.M.A. Mekhemer, M.G. Mohamed, M.H. Elsayed, K.H. Lin, Y.K. Chen, T.L. Wu, H.H. Chou, S.W. Kuo, Conjugated microporous polymers incorporating Thiazolo[5,4-d]thiazole moieties for Sunlight-Driven hydrogen production from water, *Chem. Eng. J.* 446 (2022), 137158, <https://doi.org/10.1016/j.ccej.2022.137158>.
- [10] J. Chen, B. Liu, H. Cai, S. Liu, Y. Yamauchi, S.C. Jun, Covalently interlayer-confined organic-inorganic heterostructures for aqueous potassium ion supercapacitors, *Small* 19 (2023), 2204275, <https://doi.org/10.1002/smll.202204275>.
- [11] A. Hayat, F. Raziq, M. Khan, J. Khan, S.K.B. Mane, A. Ahmad, M. Ur Rahman, W. U. Khan, Fusion of conjugated bicyclic co-polymer within polymeric carbon nitride for high photocatalytic performance, *J. Colloid Interface Sci.* 554 (2019) 627–639, <https://doi.org/10.1016/j.jcis.2019.07.048>.
- [12] Z. Cheng, L. Wang, Y. He, X. Chen, X. Wu, H. Xu, Y. Liao, M. Zhu, Rapid metal-free synthesis of pyridyl-functionalized conjugated microporous polymers for visible-light-driven water splitting, *Polym. Chem.* 11 (2020) 3393–3397, <https://doi.org/10.1039/d0py00249f>.
- [13] A.M. Elewa, A.F.M. EL-Mahdy, M.H. Elsayed, M.G. Mohamed, S.W. Kuo, H. H. Chou, Sulfur-doped triazine-conjugated microporous polymers for achieving the robust visible-light-driven hydrogen evolution, *Chem. Eng. J.* 421 (2021), 129825, <https://doi.org/10.1016/j.ccej.2021.129825>.
- [14] Z. Ajmal, T.A. Taha, M.A. Amin, A. Palamanit, W.I. Nawawi, A. Kalam, A.G. Al-Sehemi, H. Algarni, A. Qadeer, H. Ali, A. Kumar, J. Qian, H. Zeng, Embedding aromatic conjugated monomer within carbon nitride for efficient photocatalytic reduction reactions, *J. Mol. Liq.* 368 (2022), 120617, <https://doi.org/10.1016/j.molliq.2022.120617>.
- [15] W.C. Lin, M.H. Elsayed, J. Jayakumar, L.Y. Ting, C.L. Chang, A.M. Elewa, W. S. Wang, C.C. Chung, C.Y. Lu, H.H. Chou, Design and synthesis of cyclometalated iridium-based polymer dots as photocatalysts for visible light-driven hydrogen evolution, *Int. J. Hydrogen Energy* 45 (2020) 32072–32081, <https://doi.org/10.1016/j.ijhydene.2020.08.288>.
- [16] C. Han, S. Xiang, S. Jin, C. Zhang, J.X. Jiang, Rational design of conjugated microporous polymer photocatalysts with definite D- $\pi$ -A structures for ultrahigh photocatalytic hydrogen evolution activity under natural sunlight, *ACS Catal.* 13 (2023) 204–212, <https://doi.org/10.1021/acscatal.2c04993>.
- [17] J. Jayakumar, H.H. Chou, Recent advances in visible-light-driven hydrogen evolution from water using polymer photocatalysts, *ChemCatChem* 12 (2020) 689–704, <https://doi.org/10.1002/cctc.201901725>.
- [18] R. Shah, S. Ali, F. Raziq, S. Ali, P.M. Ismail, S. Shah, R. Iqbal, X. Wu, W. He, X. Zu, A. Zada Adnan, F. Mabood, A. Vinu, S.H. Jung, J. Yi, L. Qiao, Exploration of metal organic frameworks and covalent organic frameworks for energy-related applications, *Coord. Chem. Rev.* 477 (2023), 214968, <https://doi.org/10.1016/j.ccr.2022.214968>.
- [19] N.M. Gupta, Factors affecting the efficiency of a water splitting photocatalyst: a perspective, *Renewable Sustainable Energy Rev.* 71 (2017) 585–601, <https://doi.org/10.1016/j.rser.2016.12.086>.
- [20] P. Nikolaidis, A. Poullikkas, A comparative overview of hydrogen production processes, *Renewable Sustainable Energy Rev.* 67 (2017) 597–611, <https://doi.org/10.1016/j.rser.2016.09.044>.
- [21] A.E. Hassan, M.H. Elsayed, M.S.A. Hussien, M.G. Mohamed, S.W. Kuo, H.H. Chou, I.S. Yahia, T.A. Mohamed, Z. Wen, V<sub>2</sub>O<sub>5</sub> nanoribbons/N-deficient g-C<sub>3</sub>N<sub>4</sub> heterostructure for enhanced visible-light photocatalytic performance, *Int. J. Hydrogen Energy* 48 (2023) 9620–9635, <https://doi.org/10.1016/j.ijhydene.2022.12.009>.
- [22] P. Niu, M. Qiao, Y. Li, L. Huang, T. Zhai, Distinctive defects engineering in graphitic carbon nitride for greatly extended visible light photocatalytic hydrogen evolution, *Nano Energy* 44 (2018) 73–81, <https://doi.org/10.1016/j.nanoen.2017.11.059>.
- [23] J.-H. Zhang, M.-J. Wei, Z.-W. Wei, M. Pan, C.-Y. Su, Ultrathin graphitic carbon nitride nanosheets for photocatalytic hydrogen evolution, *ACS Appl. Nano Mater.* 3 (2020) 1010–1018, <https://doi.org/10.1021/acsnam.9b02590>.
- [24] L. Zhang, Z. Jin, S. Huang, X. Huang, B. Xu, L. Hu, H. Cui, S. Ruan, Y.-J. Zeng, Bio-inspired carbon doped graphitic carbon nitride with booming photocatalytic hydrogen evolution, *Appl. Catal. B Environ.* 246 (2019) 61–71, <https://doi.org/10.1016/j.apcatb.2019.01.040>.
- [25] W.-C. Lin, J. Jayakumar, C.-L. Chang, L.-Y. Ting, T.-F. Huang, M.H. Elsayed, A. M. Elewa, Y.-T. Lin, J.-J. Liu, Y.-T. Tseng, H.-H. Chou, Sulfide oxidation tuning in 4,8-bis(5-(2-ethylhexyl)thiophen-2-yl)benzo[1,2-b:4,5-b']dithiophene based dual acceptor copolymers for highly efficient photocatalytic hydrogen evolution, *J. Mater. Chem.* 10 (2022) 6641–6648, <https://doi.org/10.1039/D2TA00241H>.
- [26] A.E. Hassan, M.S.A. Hussien, M.H. Elsayed, M.G. Mohamed, S.W. Kuo, H.H. Chou, I.S. Yahia, G. Wang, Z. Wen, One-step construction of Y, C, and O tridoped g-C<sub>3</sub>N<sub>4</sub> as a bifunctional photocatalyst for H<sub>2</sub> evolution and organic pollutant degradation under visible light irradiation, *Sustain. Energy Fuels* 6 (2022) 3858–3871, <https://doi.org/10.1039/D2SE00525E>.
- [27] C. Zhang, C. Xie, Y. Gao, X. Tao, C. Ding, F. Fan, H.-L. Jiang, Charge separation by creating band bending in metal-organic frameworks for improved photocatalytic hydrogen evolution, *Angew. Chem. Int. Ed.* 61 (2022), e202204108, <https://doi.org/10.1002/anie.202204108>.
- [28] S. Wang, X. Wang, Multifunctional metal-organic frameworks for photocatalysis, *Small* 11 (2015) 3097–3112, <https://doi.org/10.1002/smll.201500084>.
- [29] W.T. Chung, I.M.A. Mekhemer, M.G. Mohamed, A.M. Elewa, A.F.M. EL-Mahdy, H. H. Chou, S.W. Kuo, K.C.W. Wu, Recent advances in metal/covalent organic frameworks based materials: their synthesis, structure design and potential applications for hydrogen production, *Coord. Chem. Rev.* 483 (2023), 215066, <https://doi.org/10.1016/j.ccr.2023.215066>.
- [30] Z. Mi, T. Zhou, W. Weng, J. Unruangsri, K.e. Hu, W. Yang, C. Wang, K.A.I. Zhang, J. Guo, Covalent organic frameworks enabling site isolation of viologen-derived electron-transfer mediators for stable photocatalytic hydrogen evolution, *Angew. Chem. Int. Ed.* 60 (2021) 9642–9649, <https://doi.org/10.1002/anie.202016618>.
- [31] Y. Li, X. Song, G. Zhang, L. Wang, Y. Liu, W. Chen, L. Chen, 2D covalent organic frameworks toward efficient photocatalytic hydrogen evolution, *ChemSusChem* 15 (2022), e202200901, <https://doi.org/10.1002/cssc.202200901>.
- [32] M.G. Mohamed, M.H. Elsayed, A.M. Elewa, A.F. EL-Mahdy, C.-H. Yang, A. A. Mohammed, H.-H. Chou, S.-W. Kuo, Pyrene-containing conjugated organic microporous polymers for photocatalytic hydrogen evolution from water, *Catal. Sci. Technol.* 11 (2021) 2229–2241, <https://doi.org/10.1039/D0CY02482A>.
- [33] L. Wang, Y. Wan, Y. Ding, S. Wu, Y. Zhang, X. Zhang, G. Zhang, Y. Xiong, X. Wu, J. Yang, Conjugated microporous polymer nanosheets for overall water splitting using visible light, *Adv. Mater.* 29 (2017), 1702428, <https://doi.org/10.1002/adma.201702428>.
- [34] S. Xiang, C. Han, C. Shu, C. Zhang, J.-X. Jiang, Structure evolution of thiophene-containing conjugated polymer photocatalysts for high-efficiency photocatalytic hydrogen production, *Sci. China Mater.* 65 (2022) 422–430, <https://doi.org/10.1007/s40843-021-1757-1>.
- [35] Y. Song, P.-C. Lan, K. Martin, S. Ma, Rational design of bifunctional conjugated microporous polymers, *Nanoscale Adv.* 3 (2021) 4891–4906, <https://doi.org/10.1039/D1NA00479D>.
- [36] X. Wang, K. Maeda, A. Thomas, K. Takanebe, G. Xin, J.M. Carlsson, K. Domen, M. Antonietti, A metal-free polymeric photocatalyst for hydrogen production from water under visible light, *Nat. Mater.* 8 (2009) 76–80, <https://doi.org/10.1038/nmat2317>.
- [37] X. Jiang, P. Wang, J. Zhao, 2D covalent triazine framework: a new class of organic photocatalyst for water splitting, *J. Mater. Chem.* 3 (2015) 7750–7758, <https://doi.org/10.1039/C4TA03438D>.
- [38] R.S. Sprick, J.-X. Jiang, B. Bonillo, S. Ren, T. Ratvijitvech, P. Guiglion, M. A. Zwiijnenburg, D.J. Adams, A.I. Cooper, Tunable organic photocatalysts for visible-light-driven hydrogen evolution, *J. Am. Chem. Soc.* 137 (2015) 3265–3270, <https://doi.org/10.1021/ja511552k>.
- [39] S. Luo, Z. Zeng, G. Zeng, Z. Liu, R. Xiao, P. Xu, H. Wang, D. Huang, Y. Liu, B. Shao, Recent advances in conjugated microporous polymers for photocatalysis: designs, applications, and prospects, *J. Mater. Chem.* 8 (2020) 6434–6470, <https://doi.org/10.1039/D0TA01102A>.
- [40] J.-S.M. Lee, A.I. Cooper, Advances in conjugated microporous polymers, *Chem. Rev.* 120 (2020) 2171–2214, <https://doi.org/10.1021/acs.chemrev.9b00399>.

- [41] A.O. Mousa, Z.I. Lin, C.H. Chuang, C.K. Chen, S.W. Kuo, M.G. Mohamed, Rational design of bifunctional microporous organic polymers containing anthracene and triphenylamine units for energy storage and biological applications, *Int. J. Mol. Sci.* 24 (2023) 8966, <https://doi.org/10.3390/ijms24108966>.
- [42] M. Ejaz, M.G. Mohamed, W.C. Chang, S.W. Kuo, Synthesis and design of hypercrosslinked porous organic frameworks containing tetraphenylpyrazine unit for high-performance supercapacitor, *J. Polym. Sci.* (2023), <https://doi.org/10.1002/pol.20230174>.
- [43] J. Jiang, Z. Liang, X. Xiong, X. Zhou, H. Ji, A carbazolyl porphyrin-based conjugated microporous polymer for metal-free photocatalytic aerobic oxidation reactions, *ChemCatChem* 12 (2020) 3523–3529, <https://doi.org/10.1002/cctc.202000199>.
- [44] M.M. Samy, M.G. Mohamed, A.F.M. El-Mahdy, T.H. Mansoure, K.C.-W. Wu, S.-W. Kuo, High-performance supercapacitor electrodes prepared from dispersions of tetrabenzonaphthalene-based conjugated microporous polymers and carbon nanotubes, *ACS Appl. Mater. Interfaces* 13 (2021) 51906–51916, <https://doi.org/10.1021/acsmi.1c05720>.
- [45] R. Dawson, A. Laybourn, R. Clowes, Y.Z. Khimiyak, D.J. Adams, A.I. Cooper, Functionalized conjugated microporous polymers, *Macromolecules* 42 (2009) 8809–8816, <https://doi.org/10.1021/ma901801s>.
- [46] Z.J. Wang, S. Ghasimi, K. Landfester, K.A. Zhang, Photocatalytic Suzuki coupling reaction using conjugated microporous polymer with immobilized palladium nanoparticles under visible light, *Chem. Mater.* 27 (2015) 1921–1924, <https://doi.org/10.1021/acs.chemmater.5b00516>.
- [47] A. Suzuki, Organoboranes in organic syntheses including Suzuki coupling reaction, *Heterocycles* 80 (2010) 15–43, [https://doi.org/10.3987/COM-09-S\(S\)Summary](https://doi.org/10.3987/COM-09-S(S)Summary).
- [48] J. Schmidt, M. Werner, A. Thomas, Conjugated microporous polymer networks via Yamamoto polymerization, *Macromolecules* 42 (2009) 4426–4429, <https://doi.org/10.1021/ma9005473>.
- [49] Z. Tan, H. Su, Y. Guo, H. Liu, B. Liao, A.M. Amin, Q. Liu, Ferrocene-based conjugated microporous polymers derived from Yamamoto coupling for gas storage and dye removal, *Polymers* 12 (2020) 719, <https://doi.org/10.3390/polym12030719>.
- [50] C. Gu, Y. Chen, Z. Zhang, S. Xue, S. Sun, K. Zhang, C. Zhong, H. Zhang, Y. Pan, Y. Lv, Electrochemical route to fabricate film-like conjugated microporous polymers and application for organic electronics, *Adv. Mater.* 25 (2013) 3443–3448, <https://doi.org/10.1002/adma.201300839>.
- [51] C. Zhang, Y. Qiao, P. Xiong, W. Ma, P. Bai, X. Wang, Q. Li, J. Zhao, Y. Xu, Y. Chen, Conjugated microporous polymers with tunable electronic structure for high-performance potassium-ion batteries, *ACS Nano* 13 (2019) 745–754, <https://doi.org/10.1021/acsnano.8b08046>.
- [52] Z. Wang, X. Yang, T. Yang, Y. Zhao, F. Wang, Y. Chen, J.H. Zeng, C. Yan, F. Huang, J.-X. Jiang, Dibenzothiophene dioxide based conjugated microporous polymers for visible-light-driven hydrogen production, *ACS Catal.* 8 (2018) 8590–8596, <https://doi.org/10.1021/acscatal.8b02607>.
- [53] Q. Liu, G. Li, Z. Tang, L. Chen, B. Liao, B. Ou, Z. Zhou, H. Zhou, Design and synthesis of conjugated polymers of tunable pore size distribution, *Mater. Chem. Phys.* 186 (2017) 11–18, <https://doi.org/10.1016/j.matchemphys.2016.06.004>.
- [54] C. Ru, T. Zhou, J. Zhang, X. Wu, P. Sun, P. Chen, L. Zhou, H. Zhao, J. Wu, X. Pan, Introducing secondary acceptors into conjugated polymers to improve photocatalytic hydrogen evolution, *Macromolecules* 54 (2021) 8839–8848, <https://doi.org/10.1021/acs.macromol.1c00705>.
- [55] L. Li, Z. Cai, Q. Wu, W.-Y. Lo, N. Zhang, L.X. Chen, L. Yu, Rational design of porous conjugated polymers and roles of residual palladium for photocatalytic hydrogen production, *J. Am. Chem. Soc.* 138 (2016) 7681–7686, <https://doi.org/10.1021/jacs.6b03472>.
- [56] C. Han, S. Xiang, M. Ge, P. Xie, C. Zhang, J.X. Jiang, An efficient electron donor for conjugated microporous polymer photocatalysts with high photocatalytic hydrogen evolution activity, *Small* 18 (2022), 2202072, <https://doi.org/10.1002/sml.202202072>.
- [57] S. Wang, P. Yang, K. Chang, W. Lv, B. Mi, J. Song, X. Zhao, Z. Gao, A new dibenzo [g,p] chrysenes derivative as an efficient anode buffer for inverted polymer solar cells, *Org. Electron.* 74 (2019) 269–275, <https://doi.org/10.1016/j.orgel.2019.07.022>.
- [58] P. Xie, C. Han, S. Xiang, S. Jin, M. Ge, C. Zhang, J.X. Jiang, Toward high-performance dibenzo[g,p]chrysenes-based conjugated polymer photocatalysts for photocatalytic hydrogen production through donor-acceptor-acceptor structure design, *J. Chem. Eng.* 459 (2023), 141553, <https://doi.org/10.1016/j.ccej.2023.141553>.
- [59] Y. Suzuki, M. Yamaguchi, R. Oketani, I. Hisaki, Isomeric effect of naphthyl spacers on structures and properties of isostructural porous crystalline frameworks, *Mater. Chem. Front.* 7 (2023) 106–116, <https://doi.org/10.1039/D2QM01091G>.
- [60] C.F. Dickinson, G.P.A. Yap, M.A. Tius, Synthesis of fluorenes and dibenzo[g,p]chrysenes through an oxidative cascade, *J. Org. Chem.* 87 (2022) 1559–1563, <https://doi.org/10.1021/acs.joc.1c02583>.
- [61] M.G. Mohamed, M.M.M. Ahmed, W.T. Du, S.W. Kuo, Meso/microporous carbons from conjugated hyper-crosslinked polymers based on tetraphenylethene for high-performance CO<sub>2</sub> capture and supercapacitor, *Molecules* 26 (2021) 738, <https://doi.org/10.3390/molecules26030738>.
- [62] M.G. Mohamed, S.V. Chaganti, S.U. Sharma, M.M. Samy, M. Ejaz, J.T. Lee, K. Zhang, S.W. Kuo, Constructing conjugated microporous polymers containing the pyrene-4,5,9,10-tetraone unit for energy storage, *ACS Appl. Energy Mater.* 5 (2022) 10130–10140, <https://doi.org/10.1021/acsaem.2c01842>.
- [63] T.H. Weng, M.G. Mohamed, S.U. Sharma, S.V. Chaganti, M.M. Samy, J.T. Lee, S. W. Kuo, Ultrastable three-dimensional triptycene- and tetraphenylethene-conjugated microporous polymers for energy storage, *ACS Appl. Energy Mater.* 5 (2022) 14239–14249, <https://doi.org/10.1021/acsaem.2c02809>.
- [64] M.G. Mohamed, S.V. Chaganti, M.S. Li, M.M. Samy, S.U. Sharma, J.T. Lee, M. H. Elsayed, H.H. Chou, S.W. Kuo, Ultrastable porous organic polymers containing thianthrene and pyrene units as organic electrode materials for supercapacitors, *ACS Appl. Energy Mater.* 5 (2022) 6442–6452, <https://doi.org/10.1021/acsaem.2c00942>.
- [65] H. Yao, L. Ye, H. Zhang, S. Li, S. Zhang, J. Hou, Molecular design of benzodithiophene-based organic photovoltaic materials, *Chem. Rev.* 116 (2016) 7397–7457, <https://doi.org/10.1021/acs.chemrev.6b00176>.
- [66] P. Leung, J. Bu, P.Q. Velasco, M.R. Roberts, N. Grobert, P.S. Grant, Single-Step spray printing of symmetric all-organic solid-state batteries based on porous textile dye electrodes, *Adv. Energy Mater.* 9 (2019), 1901418, <https://doi.org/10.1002/aenm.201901418>.
- [67] W. Sun, Y. Xiang, Z. Jiang, S. Wang, N. Yang, S. Jin, L. Sun, H. Teng, H. Chen, Designed polymeric conjugation motivates tunable activation of molecular oxygen in heterogeneous organic photosynthesis, *Sci. Bull.* 67 (2022) 61–70, <https://doi.org/10.1016/j.scib.2021.07.016>.
- [68] S. Wang, X. Hai, X. Ding, S. Jin, Y. Xiang, P. Wang, B. Jiang, F. Ichihara, M. Oshikiri, X. Meng, Y. Li, W. Matsuda, J. Ma, S. Seki, X. Wang, H. Huang, Y. Wada, H. Chen, J. Ye, Intermolecular cascaded  $\pi$ -conjugation channels for electron delivery powering CO<sub>2</sub> photoreduction, *Nat. Commun.* 11 (2020) 1149, <https://doi.org/10.1038/s41467-020-14851-7>.
- [69] Y. Zhang, D. Yi, P. Tu, S. Yang, Q. Xie, Z. Gao, S. Wu, G. Yu, Boosting radioactive iodine capture of microporous polymers through strengthened host-guest interaction, *Microporous Mesoporous Mater.* 321 (2021), 111148, <https://doi.org/10.1016/j.micromeso.2021.111148>.